Quim. Nova, Vol. 46, No. 2, 157-167, 2023 http://dx.doi.org/10.21577/0100-4042.20170969

Artigo

MESOPOROUS SILICA DECORATED WITH SILVER NANOPARTICLES – AN INVESTIGATION OF THE RADIOLYTIC SYNTHESIS PARAMETERS THROUGH FACTORIAL EXPERIMENTS

Clara Lana Bispo Fidelis[a], Marcelo Fernandes Cipreste[a,#], Pedro Lana Gastelois[a], Waldemar Augusto de Almeida Macedo[a] and Edésia Martins Barros de Sousa[a,*]

[a]Laboratório de Materiais Nanoestruturados para Bioaplicações, Centro de Desenvolvimento da Tecnologia Nuclear, 31270-901 Belo Horizonte – MG, Brasil

Recebido em 20/06/2022; aceito em 30/09/2022; publicado na web em 09/12/2022

Resistant infectious microorganisms are causing a worldwide emerging problem, called antimicrobial resistance. To avoid this outbreak, new antimicrobial technologies are necessary. Silver nanoparticles (AgNPs) are known for their antibacterial properties and several studies have focused on their synthesis, characterization, and biological assays. One possibility to synthesize AgNPs is through gamma radiation, known as radiolytic synthesis. This work focuses on the radiolytic synthesis of AgNPs capped into a mesoporous silica nanoparticle aiming at an antimicrobial application. The variants of the radiolytic synthesis, which may influence the AgNPs formation, were studied and statistically compared by Design of Experiments Factorial Design in Minitab Software. The Ag content is statically dependent on dose, volume, and pH, as well as on two parameters interaction: [Ag+]-pH and [Ag+]-volume-pH interaction. Transmission electron microscopy and nitrogen adsorption analyses indicated the presence of subnanometric AgNPS located inside the mesopores. Silver nanoagglomerates were also found by transmission electron microscopy, which could be formed by silver oxides, as shown in X-ray photoelectron spectroscopy. AgNPs reduce the specific surface area of the silica nanoparticle, while the matrix morphology remains. The nanocomposites presented preliminary biocompatibility observed in *in vitro* biological assay using fibroblasts, which support their application in biological systems as antimicrobial substitutes.

Keywords: silver nanoparticles; mesoporous silica nanoparticles; radiolytic synthesis; antimicrobial resistance.

INTRODUCTION

Antimicrobial resistance (AMR) is a global emerging problem. It is estimated to cause 700,000 deaths per year.[1] The World Health Organization (WHO) alerts about the AMR rising and a global action plan has been defined in 2015.[2] One of the goals of this plan is the increase of the research and development of new antimicrobials, diagnostics, and alternative approaches to fighting superbugs. Nanobiotechnology is increasingly been considered to solve the AMR problem due to the possibility to engineer multifunctional antimicrobial nanosystems, creating drug-delivery carriers[3–6] and/or bacteria targeting nanoparticles.[7–9] Moreover, fighting AMR with metal nanoparticles, such as silver nanoparticles (AgNPs), is an efficient strategy.[10–12]

AgNPs are known for their antibacterial properties for decades, and several studies have focused on their synthesis, characterization, and biological assays.[13–18] Despite the antimicrobial properties, AgNPs are widely studied owing to their excellent physical-chemical, optical, electrical, and magnetic properties, which differ from their bulk form.[19]

The metallic nanoparticle's synthesis, including AgNPs, is based on the reduction of metallic salts by physical, chemical, or biological processes.[20] Physical methods based on high-energy ionizing radiation, such as gamma radiation, present some advantages, *e.g.*, reduction of synthesis time and temperature, elimination of hazardous reducing agents, control of particle nucleation and growth by controlling the synthesis parameters.[21,22]

In radiolytic synthesis, occurs the solvent radiolysis, usually water, promoted by the radiation source. The water radiolysis is already established and well described in literature since the 1960s.[23] The water ionization produces excited water molecules (H_2O^*), H_2O^+ ions, and secondary electrons (e^-). These species are responsible for the subsequent radical's generation, such as hydrogen radicals (H•), hydroxyl radicals (OH•), hydronium ion (H_3O^+), and solvated electrons (e^{-aq}).[24] In the second stage of the synthesis, the reduction of the metallic ions occurs through the strong reducing agents produced: e^{-aq} and H•. On the other hand, the OH• radical is an oxidizing agent. Therefore, it is fundamental to use a scavenger agent, for instance, primary or secondary alcohols. Lastly, once the metal atoms are synthesized, they tend to interact by gowning a cluster, due to their high surface energy. Therefore, a stabilizer is required to avoid the particles coalescence.[19-22,24] Several studies report the use of polymers,[25-27] ligands,[28] and inorganic supports.[29-32]

The radiolytic synthesis parameters, *e.g.*, radiation dose, dose rate, pH, stabilizer, and precursor concentration, are key factors in the formation of the nanoparticles in terms of average size and size distribution, reduction yield, and stability. Several authors focused on discussing these parameters effects.[21,22,33,34] However, it has never been reported a full factorial design of experiments, varying four parameters to evaluate response.

In this work, we report on the radiolytic synthesis of AgNPs and a statistical study of the synthesis parameters using Minitab Statistical Software. With Factorial Design, a tool of Minitab's Design of Experiments (DOE), it is possible to simultaneously vary different factors and investigate their effects on a process, as well as the influence of the interaction. Without factorial designs, important interactions can be undetected. The parameters varied in this study were the radiation dose, $[Ag^+]$ precursor, suspension volume, and pH.

The AgNPs were stabilized into mesoporous silica nanoparticles (MSN) MCM-41 matrix. Inorganic supports can be used to cap recently formed AgNPs.[14,15,18] Aiming for biomedical applications, the use of MSN is promising due to its large surface area, uniform pore size distribution, high pore volume, good biocompatibility, and

*e-mail: sousaem@cdtn.br
#Current address: JHS Biomateriais. Rua Ouro Branco, 345 – Sabará/MG

a surface that allows further chemical functionalization.[35] Besides, being a support to AgNPs formation, the MSN can reduce the AgNPs cytotoxicity, while controls the Ag^+ releases.[5] The use of MCM-41 as drug carriers was first reported by the Vallet-Regí Group in 2001[36] and since then this important nanomaterial has been explored as a candidate for drug-delivery systems. Therefore, the MCM-41 decorated with AgNPs presented in this work is a strong candidate for antimicrobial treatment.

MATERIALS AND METHODS

Materials

Hexadecyltrimethylammonium bromide (CTAB), sodium hydroxide (NaOH), tetraethylorthosilicate (TEOS), and silver nitrate ($AgNO_3$) were purchased from Sigma-Aldrich. 2- propanol (C_3H_8O) was supplied by Merck. Analytical solvents used in the assays were obtained from Synth and Fmaia. Water solutions were prepared with purified water obtained from Milli-Q® Direct Water Purification System (Millipore - Burlington, USA).

For the biological assay, Dulbecco's Modified Eagle Medium (DMEM) and fetal bovine serum (FBS) were purchased from Sigma-Aldrich. MTT (3-(4,5-Dimethylthiazol-2-yl)-2,5-Diphenyltetrazolium Bromide) (Invitrogen™) and Trypsin/EDTA Solution (Gibco™) was acquired from Thermo Fisher Scientific.

Synthesis of mesoporous silica MCM-41

MCM-41 silica was prepared according to our previous work.[35,37] CTAB (1.00 g) was dissolved in a 480 mL NaOH (280 mg) solution under constant stirring at 78 ºC. TEOS (5.00 mL) was added dropwise, and the mixture was kept under heating and stirring for 2 h. The resulting white solid was centrifuged, washed with water and ethanol, and dried at 60 ºC for 24 h. The surfactant was removed by calcination at 575 ºC for 5 h in air.

Synthesis of AgNPs by gamma radiation

Due to the lack of published work using MSN as a support to the gamma reduced AgNPs, we based our protocol on Ramnani and collaborator's work, adding several adjustments.[29] Moreover, the radiolytic synthesis parameters (dose, $AgNO_3$ concentration, volume, and pH) were varied in order to study their effects on the formed nanocomposites.

In a typical procedure, Millipore H_2O, MCM-41 (0.05% (w/v)) and $AgNO_3$ were mixed at room temperature. An amount of 2-propanol relative to $AgNO_3$ was added as a scavenger agent. NaOH was used to adjust the suspension pH. To obtain a well-dispersed colloidal suspension, the mixture was kept in an ultrasound bath for 30 minutes. The suspension (100 to 200 mL) was irradiated with a ^{60}Co source (1 to 4 kGy) in the Gamma Irradiation Laboratory at CDTN. The resulting suspensions were filtered and abundantly washed with water. The final solids were dried at room temperature for 24 h.

Factorial Design

To investigate the effect of the aforementioned synthesis parameters, it was created a factorial design experiment of 4 factors, *i.e.* 2^4, with a central point (17 runs) by Minitab® using DOE. The 4 analyzed factors were dose (1 to 4 kGy), [$AgNO_3$] (2.0 to 4.0 mM), irradiated volume (100 to 200 mL), and pH (7 to 10). The response data needed to analyze was the Ag content (wt%) obtained by ICP-OES.

Nanocomposites nomenclature

Since it is reported that 17 different nanocomposites, a nomenclature system was required. In general, a nanocomposite is named according to Figure 1. For example: MCM-Ag-4-7 is the nanocomposite irradiated with 4 kGy, [Ag^+] = 2 mM, volume = 100 mL and pH = 7. A final nanocomposite without pH adjustment, *i.e.* without adding NaOH during synthesis, was prepared and named MCM-Ag-4.

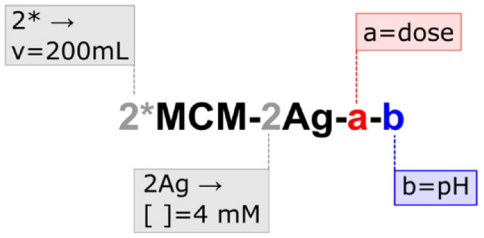

Figure 1. *MCM-Ag nanocomposite's nomenclature*

Characterizations

The samples were characterized by UV-Visible spectroscopy (UV-Vis), inductively coupled plasma optical emission spectroscopy (ICP-OES), Fourier transform infrared spectroscopy (FTIR), X-ray diffraction (XRD), N_2 adsorption, transmission electron microscopy (TEM), scanning electron microscopy (SEM), X-ray photoelectron spectroscopy (XPS) and zeta potential analysis.

UV-Vis (Shimadzu model UV-2550) was conducted to identify the region of the electromagnetic spectrum where occurs absorption bands, which are related to the surface plasmon resonance (SPR) from AgNPs. The suspension was prepared with a concentration of 0.167 mg mL^{-1} and it was dispersed with an ultrasound tip until the energy reach 15 kJ. About 4 mL of these prepared suspensions were poured on quartz cuvettes with 10 mm of path length, and the absorption spectra were taken from 200 to 800 nm. ICP-OES (Spectro ARCOS) was used to determine the Ag content in each nanocomposite. The equipment measured an [Ag] of a prepared solution containing ±1mg of sample and 10 mL of HNO_3 (37.5%). The nanocomposites Ag content (wt%) was then calculated. The FTIR (BRUKER model VERTEX 70v) procedure was conducted to identify the chemical bonds present in the materials. The measurements were made with attenuated total reflection (ATR) mode using a diamond crystal, with 64 runs ranging from 4000 and 100 cm^{-1} and a resolution of 4 cm^{-1}. XRD (Rigaku model Ultima IV) patterns were taken to characterize the AgNPs. The samples were tested with irradiation angles from 10° to 80° at a 0.2° min^{-1} rate. The X-ray radiation was generated using a 2 kW copper tube and only the Cu-Kα characteristic radiation (λ = 1.5406 Å) was used for analysis. The Ag crystallites sizes were calculated using the Debye-Scherrer equation ($D=K\lambda/\beta\cos\theta$), where: D = average crystallite size, λ = X-Ray wavelength, β = line broadening in radians, and θ = Bragg angle. N_2 adsorption-desorption isotherms were obtained using a Quantachrome Nova 2200 adsorption analyzer. Before the adsorption measurements, the materials were out-gassed for 4 h at 300 ºC (MCM-41) and 12 h at 80 ºC (nanocomposites). The data analyses were performed using the NovaWin V.10, 1997e2007 Quantachrome Instruments software (Boynton Beach, FL, USA). The specific surface area was determined by the Brunauer-Emmett-Teller (BET) method at -196 ºC.[38] The specific pore diameters and pore volumes were determined by the density functional theory (DFT) method.[39] The microscopy images were taken to characterize samples morphology. SEM was performed with a Quanta 200-FEG-FEI-2006 equipment and TEM images were

obtained in a FEI TECNAI G2 microscope operating at 200 Kv. The samples were dispersed in water (0.1 mg mL^{-1}) for 30 minutes using an ultrasonic bath. One drop was placed onto a silicon substrate and then exposed to a gold sputtering (for SEM) and onto a 200 mesh holey carbon copper grid (for TEM). XPS was used to analyze the material's surface composition and oxidation state. The spectra were obtained using monochromatic Al-Kα X-rays (1486.6 eV) as the excitation source, and a Phoibos-150 (Specs) electron-energy analyzer. The survey spectra were acquired with 1 eV of energy step and 50 eV of pass energy, whereas the high-resolution spectra, in the region of the Ag 3d photoemission peak (~368 eV), were acquired using 0.1 eV of energy step and 30 eV of pass energy. The high-resolution spectra were fitted using the Casa XPS software with the convolution of Lorentzian and Gaussian distributions and Shirley background correction. Adventitious carbon C1 s peak at 284.6 eV was used to correct the binding energy (BE) scales. The surfaces' chemical compositions were obtained from the integration of the area under each peak, corrected by the sensitivity factor associated with each correspondent element. Similarly, the proportion of the element's chemical states was evaluated by integrating the areas under the fitted curves centered on the energies associated with each chemical bond (or oxidation state of the element). Finally, zeta potential analysis was conducted in a Zetasizer Nanoseries Zs (Malvern Instruments) apparatus after the samples had been adequately dispersed in water (0.1 mg mL^{-1}) using an ultrasound tip until the energy reach 5 kJ.

Biological assay

Cell culture

Human fibroblasts cells (MRC-5) were cultivated at 37 °C, with 95% humidity, and 5% CO_2 in cell culture flasks with DMEM containing 10% FBS, weekly split by trypsinization when the cell population reached 70% confluence.

Cell availability assay

The nanoparticles' biocompatibility was investigated by MTT assays. For the MTT assay, MRC-5 cells were seeded (5.0×10^3 cells/well) on 96-well plates. After 24 h incubation, cells were treated with the materials in 3 concentrations (50, 100, and 200 μg mL^{-1}). Experiments were performed in triplicate with 3 blank and 3 control wells. After another 24 h of incubation, the media of the wells were removed and washed with phosphate-buffered saline (PBS). Following, 10 μL of MTT solution (5 mg mL^{-1}) and 90 μL of DMEM were added per well. The plates were incubated for 4 h until the formazan crystallization and 100 μL of dimethyl sulfoxide (DMSO) were added to dissolve the formazan crystals. The absorbance was measured at 570 nm using a Multiskan GO microplate reader (Thermo Scientific, USA). The absorbance from blank wells was subtracted from each measurement and the cell viability was calculated as a function of the control group absorbance.

RESULTS AND DISCUSSION

UV-Vis analysis informs about the presence of AgNPs due to the Surface Plasmon Resonance (SPR). SPR is a phenomenon observed in noble metal nanoparticles, such as silver and gold, in which the conduction band electrons, coming from the valence layer d, can oscillate when exposed to a specific wavelength, creating a resonance.[40] The resonance condition depends on the nature of the nanoparticle, its size, and shape. In the case of spherical silver AgNPs, the SPR occurs around 410 nm.[25,27,28]

Figure 2 shows the UV-Vis spectra of all 18 samples (17 nanocomposites from factorial design plus MCM-Ag-4). The graphs are divided by colors, according to synthesis parameters, and in each condition, the samples were irradiated with 1 or 4 kGy. The dashed curves represent samples irradiated with 1 kGy and the solid curves, 4 kGy. This result suggests the AgNPs formation in all nanocomposites, once the SPR absorbance band was observed in all cases.

Moreover, the increase in dose promotes a higher reduction of AgNPs, therefore a bigger area under the SPR band is expected.[25,29] Comparing each graph individually, it is clear that 4 kGy (solid curves) boosts the AgNPs formation. On the order hand, a blue shift of SPR absorbance is expected when the nanoparticles diameter decrease as a result of the dose increase.[27] However, this tendency was not observed in our results.

Before irradiation, the suspension was colorless and did not show any absorption band (Figure 1S A, Supplementary Material), which means that Ag^+ ions, coming from silver nitrate, do not resonate with light, as predicted.[25] Additionally, solutions containing silver nitrate but any MSN were also irradiated, in order to study the stabilizer influence on AgNPs formation. The irradiated silver does not show any absorbance (Figure 1S B, Supplementary Material) due to the agglomeration of recently formed particles. This indicates the importance of the stabilizing agent, such as silica, for obtaining stable AgNPs.

The silver content (wt%) of the 18 nanocomposites was obtained by ICP-OES analysis and the results are shown in Table 1. The colors follow the name pattern as in UV-Vis results, according to synthesis parameters. Each color has two nanocomposites with the same chemical conditions, varying only the dose (1 to 4 kGy). Considering the aforementioned pairs, the Ag content (wt%) increased with dose in all cases, in agreement with UV-Vis results. The applied radiation dose is a key factor in terms of radiolytic synthesis. Several studies in the literature compare the dose-effect in terms of formed AgNPs.[25,29,41]

The solvated electrons formed during water radiolysis reduce Ag^+ ions into Ag^0, as described in Eq (1).[28] The metallic silver, once it is formed, starts to coalesce and form nanoaggregates, due to their high surface energy, as shown in Eq (2) and Eq (3).[27] The dose increase generates more solvated electrons and, therefore, increases the ionic silver reduction,[25] as observed in the presented result. Additionally, a dose increase can also decrease the AgNPs average size,[27,41] which was not evident in our result.

$$Ag^+ + e^-_{aq} \rightarrow Ag^0 \quad (1)$$

$$Ag^0 + Ag^0 \rightarrow Ag_2 \quad (2)$$

$$Ag_m + Ag_n \rightarrow Ag_{m+n} \quad (3)$$

The hydroxyl radicals are captured by isopropyl alcohol, the scavenger agent, forming isopropyl radicals (Eq (4) and Eq (5)). These recently formed radicals act as reducing agents and can also contribute to silver reduction, as shown in Eq (6).[34]

$$OH\bullet + CH_3CHOHCH_3 \rightarrow H_2O + H_3CC \bullet OHCH_3 \quad (4)$$

$$H\bullet + CH_3CHOCCH_3 \rightarrow H_2 + H_3CC \bullet OHCH_3 \quad (5)$$

$$Ag^+ + H_3CC \bullet OHCH_3 \; CH_3COCH_3 + Ag^0 + H^+ \quad (6)$$

Diversely, the other factors, *i.e.* [Ag^+], volume, and pH had a less evident influence on the Ag content (wt%). Therefore, it is necessary to discuss the literature's evidence about them. Firstly, considering the increase in [Ag^+], expressed by samples containing the term "2Ag". The increase in precursor concentration can increase the AgNPs average size.[26,27] This can be caused due to the ions increase, which stimulate their association rate, and also due to the reduction of capping yield from the stabilizers.[20] Nevertheless, there is a difference between AgNPs size and Ag content (wt%).

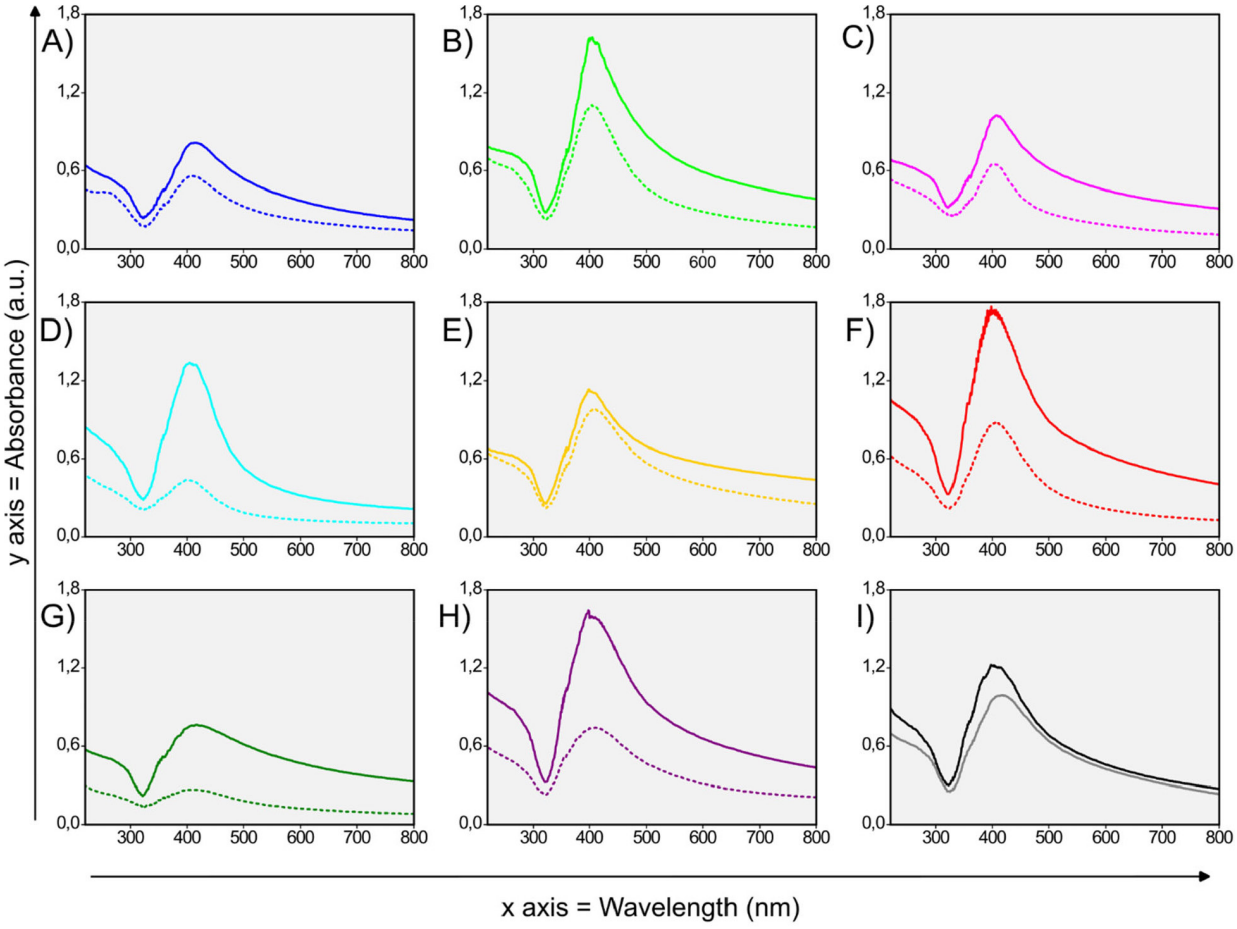

Figure 2. *UV-Vis absorbance spectra of 18 nanocomposites. Graph A (blue curve): MCM-Ag-a-7. Graph B (green curve): MCM-2Ag-a-7. Graph C (magenta curve): 2*MCM-Ag-a-7. Graph D (cyan curve): 2*MCM-2Ag-a-7. Graph E (yellow curve) MCM-Ag-a-10. Graph F (red curve) MCM-2Ag-a-10. Graph G (olive curve) 2*MCM-Ag-a-10. Graph H (purple curve) 2*MCM-2Ag-a-10. Graph I: black curve corresponds to Central Point and gray curve to MCM-Ag-4. The dashed curves are the nanocomposites synthesized with 1 kGy (a = 1) and the solid curves, with 4 kGy (a = 4)*

Table 1. Silver content in wt% according to ICP-OES analysis of the 17 factorial designed nanocomposites and MCM-Ag-4

Nanocomposite	Ag content (wt%)
MCM-Ag-1-7	4.80
MCM-Ag-4-7	9.13
MCM-2Ag-1-7	8.80
MCM-2Ag-4-7	21.75
2*MCM-Ag-1-7	2.53
2*MCM-Ag-4-7	11.21
2*MCM-2Ag-1-7	2.00
2*MCM-2Ag-4-7	7.51
MCM-Ag-1-10	13.07
MCM-Ag-4-10	20.99
MCM-2Ag-1-10	5.96
MCM-2Ag-4-10	12.94
2*MCM-Ag-1-10	2.13
2*MCM-Ag-4-10	12.35
2*MCM-2Ag-1-10	7.35
2*MCM-2Ag-4-10	14.36
Central Point	7.15
MCM-Ag-4	5.27

Secondly, the influence of pH is known to affect radiolytic synthesis.[21] Ramnani *et al.* concluded that AgNPs formed in acidic and neutral media have similar sizes, but in alkaline media, they are not stable.[29] Dhayagude *et al.*, on the other hand, found that alkaline pH leads to the formation of silver nanoplates.[25] The Ag content as a function of pH, however, may vary according to the experimental condition of each work.

Considering the high amount of data, the statistical analysis with Minitab® factorial design analysis contributed to determining the relevant factors in the response (Ag content). This tool allows the calculation of interactions between factors, which can be the driving force in many processes. Without factorial design analysis, important interactions can remain not detected. In a full factorial design, responses are measured at all combinations of experimental factor levels.[42]

Figure 3 shows the Minitab factorial design plots. On the Pareto chart (Figure 3A), bars that cross the reference line are statistically significant. It means factor A (dose), BCD ([Ag^+]-volume-pH interaction), C (volume), D (pH) and BD ([Ag^+]-pH interaction) are statistically significant. On the normal probability plot of the effects (Figure 3B), effects that are further from 0 are statistically significant. In addition, the plot indicates the direction of the effect. Effects A, BCD, and D are positive, *i.e.*, they increase the response. Effects BD and C are negative, *i.e.*, they decrease the response. This analysis reveals [Ag^+] does not individually influence the Ag content, but its interaction with other factors, for instance, volume and pH, is statistically significant.

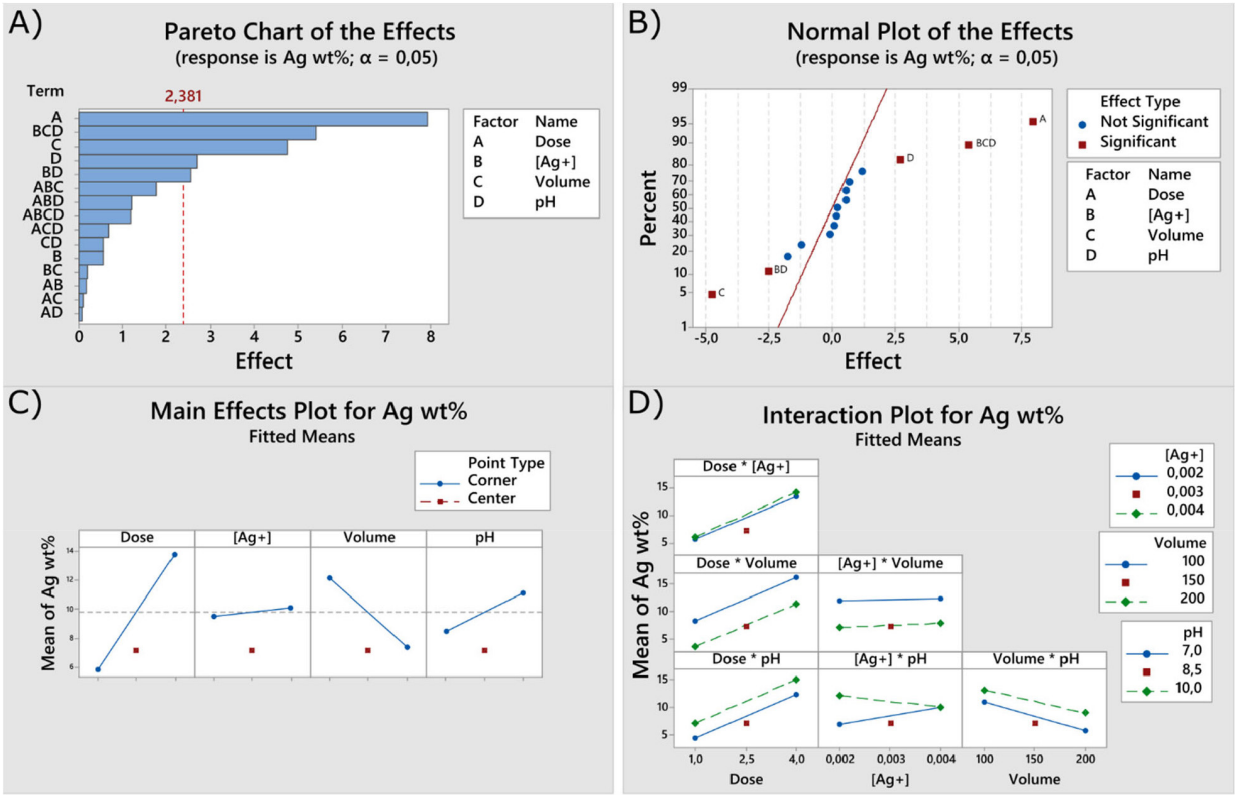

Figure 3. *Minitab factorial design plots: A) Pareto Chart, B) Normal Plot, C) Main Effect Plot, and D) Interaction Plot*

The main effects plots (Figure 3C) show the fitted means for each level of each categorical variable. The Ag content (wt%) raises in the function of dose and pH, declines in function of volume, and remains constant in the function of [Ag^+]. The interaction plot (Figure 3D), a unique tool of factorial design, exhibits the fitted mean of Ag content (wt%) in the function of factors the combined 2 by 2, *i.e.*, an average of one level while the other is held constant. The nonparallel lines on the [Ag^+]-pH interaction plot indicate interaction effects between them. At pH 7, the Ag content (wt%) increases in function of [Ag^+] raise, whereas at pH 10, the Ag content (wt%) decreases with [Ag^+] raise. A hypothesis for the observed behavior could be that there may be a greater silver oxide (Ag_2O) formation at alkaline pH and higher [$AgNO_3$], caused by NaOH excess. The formed oxide precipitated during suspension preparation; therefore, it was not caped by MSN, which resulted in a lower Ag content (wt%) nanocomposite. Nishimura *et al*. proposed that AgNPs formation increased when NaOH was added during synthesis. According to them, even though NaOH causes Ag_2O precipitation at room temperature, the oxide was further dissolved by heating, promoting a [Ag^+] raise and, thus, AgNPs nucleation.[43] In this work, the pH is clearly causing an important impact on Ag content. Comparing the nanocomposites MCM-Ag-4 (with no NaOH addiction) and MCM-Ag-4-10, the Ag content rises from 5.27 wt% to 20.99 wt%. However, the reaction kinetics in an alkaline medium is still unclear.

At least, taking the Central Point into account (Figure 3C) it is noticeable that it is lower than the Ag content (wt%) average level. It means that the response surface presents a significant curvature, *i.e.*, the response is non-linear.

Figure 4A shows FTIR spectra of MCM-41 and 3 different nanocomposites. The gray dashed lines were demarcated to characterize typical silica IR bands. The nanocomposites presented the same IR bands as pure MCM-41. The highlighted numbers in the chart are referring to: 1) bending (δ) band assigned to physiosorbed water molecules at 1630 cm^{-1}, 2) symmetric stretching band belonging to Si-O-Si at approximately 1065 cm^{-1}, 3) symmetric stretching band assigned to Si-O-H from the superficial silanol groups at approximately 960 cm^{-1}, 4) bending (δ) band assigned to Si-O at approximately 800 cm^{-1}, and 5) bending (γ) band assigned to Si-O-Si at approximately 455 cm^{-1}. The broad band between 3600 and 3000 cm^{-1} is attributed to stretching of O-H, coming from physiosorbed water or silanol groups.[35,37,44]

XRD patterns are presented in Figure 4B. The nanocomposites diffractograms present a broad halo around 2θ = 23° corresponding to the silica matrix, which is an amorphous ceramic. The sharp and well-defined peaks observed at 2θ = 38.25°, 2θ = 44.31°, 2θ = 64.61° and 2θ = 77.55° correspond to the reflection planes (111), (200), (220), (311), respectively, assigned to the FCC metallic Ag. The peaks are according to an ICDD database pattern No 4-783 and the literature.[4,5,29,45] Hence, it is possible to confirm the presence of metallic silver, even in nanocomposite prepared at pH 10. The Ag crystallite size was calculated by the Debye-Scherrer equation and it was found the values of 18.73 nm, 17.60 nm, and 12.53 nm for MCM-Ag-4-7, MCM-Ag-4-10, and MCM-Ag-4, respectively. The Ag crystallite size was lower when no NaOH was added during synthesis. The diffraction peaks of silver oxides were not identified in any nanocomposite.

Nitrogen adsorption results are shown in Table 2 and Figure 2S (Supplementary Material). MCM-41 presents a high specific surface area (SSA) of 1117.04 $m^2\ g^{-1}$, which is consistent with the mesoporous silica state of art.[46,47] MCM-41 pores have an average size of 3.54 nm with a narrow distribution. The pore volume, in turn, is 0.74 $cm^3\ g^{-1}$. These results are in accordance with the literature.[48]

On the other hand, the nanocomposites analyzed were 2*MCM-2Ag-1-7, 2*MCM-2Ag-4-7, 2*MCM-2Ag-1-10 and 2*MCM-2Ag-7-10. Hence, we were able to analyze the effect of the AgNPs presence on the nitrogen adsorption results, as well as the effect of dose and pH. Results are also shown in Table 2 and Figure 2S (Supplementary Material). Taking the nanocomposites synthesized

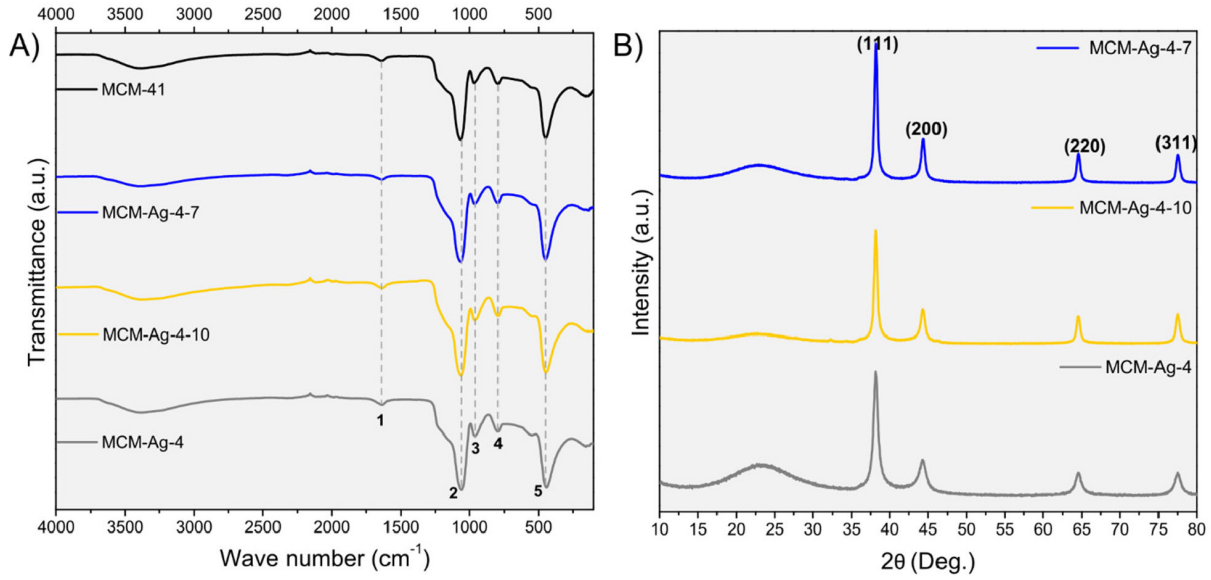

Figure 4. *A) FTIR spectra of the samples*

at pH 7 into account (2*MCM-2Ag-1-7 and 2*MCM-2Ag-4-7), it is noted that with dose increase, the SSA decreased from 1270.88 to 683.59 $m^2\ g^{-1}$, while the pore volume decreased from 0.73 to 0.42 $cm^3\ g^{-1}$. The Ag content (wt%) determined by ICP-OES of these samples increased by 2.00% to 7.51%, respectively. Pore size, on the other hand, remains the same. This indicates that AgNPs are located inside the matrix mesopores, an analysis consistent with the literature.[4,15] The 2*MCM-2Ag-1-7 sample has a very small Ag content, therefore its SSA is similar to pure MCM-41.

Conversely, considering the samples synthesized at pH 10 (2*MCM-2Ag-1-10 and 2*MCM-2Ag-4-10), the dose increases also result in a decrease in SSA from 675.22 to 450.14 $m^2\ g^{-1}$, and the pore volume from 0.36 to 0.24 $cm^3\ g^{-1}$. The Ag content of these samples are 7.35% and 14.36%, for 2*MCM-2Ag-1-10 and 2*MCM-2Ag-4-10, respectively. Once again, the increase in Ag content promotes a decrease in the SSA and pore volume, reinforcing the hypothesis that AgNPs are located inside the mesopores.

The presence of AgNPs, therefore, causes a decrease in the material's SSA. Hornebecq *et al*. reported that MCM-41 SSA decreases with the presence of AgNPs synthesized by gamma radiation.[32] The authors also consider that the AgNPs size increase promotes a greater decrease in the SSA and pore volume. Furthermore, it can be concluded that increasing the dose, as well as changing the pH from 7 to 10, leads to an increase in the Ag content, which causes a decrease in the SSA and pore volume.

Finally, all 4 nanocomposites, as well as the pure MCM-41, presented type IV isotherms with an H4 type hysteresis loop, high SSA, and a narrow pore-size distribution that are common findings for the mesoporous silica MCM-41.[38,49] This indicates that the mesoscopic structure of MCM-41 was maintained even with AgNPs formation.

Scanning electron microscopy (SEM) and transmission electron microscopy (TEM) images characterize the material's morphology. In Figure 5, it is presented the electron microscopy images of pure MCM-41. Figure 5A shows the SEM image and we can observe the silica nanoparticles spherical shape. Its average particle diameter, measured by Quantikov Software,[50] is 134±26 nm and the median value is 130 nm (Figure 5B). TEM image, shown in Figure 5C, characterizes the ordered mesopore structure of MCM-41. It is possible to see a channel structure of the mesopores with parallel stripes and regions with hexagonally packed light dots, highlighted in red, observed when the electron beam was perpendicular to the main axis. The hexagonal mesopores structure was also confirmed by Small Angle X-ray scattering (SAXS). MCM-41 presented three small-angle XRD peaks, which correspond to the (100), (110), and (200) planes (Figure 3S, Supplementary Material).[35,37] The illustration in Figure 5D represents the periodical, well-organized hexagonal array of MCM-41, as shown in the TEM image. The morphology and particle size of MCM-41 are in agreement with previous work from our group.[35]

TEM images of the nanocomposites (A) MCM-Ag-4-7, (B) MCM-2Ag-4-7, and (C) MCM-Ag-4-10 are shown in Figure 6. Thicker regions or regions with higher atomic numbers of elements will appear darker, since a greater proportion of incident electrons is scattered, thus decreasing the intensity of the direct beam.[35] The images in the first line show small black dots dispersed in the silica matrix, indicating the presence of subnanometric AgNP with an average size of < 5 nm. It is suggested that these AgNPs are located inside the mesopores, once the SSA decrease with AgNPs was formed.

On the other hand, the images in the second line show bigger black dots, which are attributed to silver agglomerates of variable sizes. These agglomerates are located on the matrix surface and could be composed of silver oxide. The nanocomposite MCM-Ag-4-10 showed a bigger amount of these agglomerates, probably due to the higher amount of NaOH used during synthesis. All 3 samples showed both types of silver morphologies, as described, indicating heterogeneity during AgNPs formation.

Table 2. Nitrogen adsorption results. Specific Surface Area (SSA), pore diameter and pore volume of MCM-41, 2*MCM-2Ag-1-7, 2*MCM-2Ag-4-7, 2*MCM-2Ag-1-10 and 2*MCM-2Ag-4-10

	MCM-41	2*MCM-2Ag-1-7	2*MCM-2Ag-4-7	2*MCM-2Ag-1-10	2*MCM-2Ag-4-10
SSA ($m^2\ g^{-1}$)	1117.04	1270.88	683.59	675.22	450.14
Pore Diameter (nm)	3.54	3.30	3.30	2.70	2.70
Pore Volume ($cm^3\ g^{-1}$)	0.74	0.73	0.42	0.36	0.24

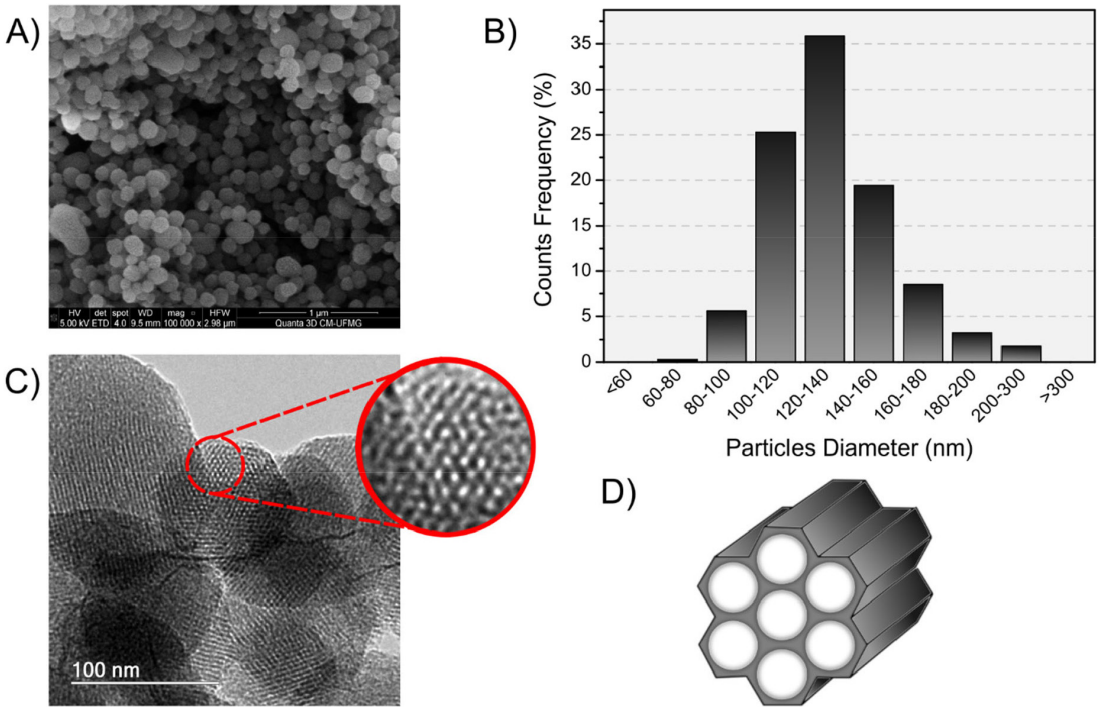

Figure 5. *Morphology of MCM-41: A) SEM image, B) particle size distribution, C) TEM image and D) Illustration of MCM-41 hexagonal mesopores distribution*

Figure 6D to Figure 6F shows TEM images of the MCM-Ag-4 nanocomposite. Figure 6D is a brightfield image with silver nanoclusters distributed with more uniform sizes than other nanocomposites. It suggests that the NaOH absence during the radiolytic synthesis may lead to a uniform AgNPs formation. In Figure 6E, a selected area electron diffraction (SAED) analysis is shown. The diffraction rings were observed, indicating a polycrystalline structure.[51,52] The distances from its edge to the center were measured using Quantikov software in order to compare with the dhkl distances of crystalline silver diffraction planes. Indeed, the planes (111), (200), (220), (311), and (222) were demarcated, since the distances from the diffraction points to the center coincided with the interplanar distances of FCC Ag, according to the ICDD database pattern No 4-783 and the literature.[53,54] This analysis confirms the XRD study (Figure 4B). Lastly, Figure 6F presents a high-resolution image (HRTEM) of a single AgNP. HRTEM image is formed by both primary and diffracted beams, simultaneously. This generates an interference pattern, where the lattice fringes are visible for crystalline materials, such as silver, making it possible to identify the crystal structure and crystallographic orientation of the sample.[55]

X-ray photoelectron spectroscopy (XPS) was used to characterize the chemical composition and to investigate the oxidation of Ag at the surface of the nanocomposites MCM-Ag-4-7, MCM-Ag-4, MCM-Ag-1-10, and MCM-Ag-4-10. The XPS survey spectra, shown in Figure 7A to Figure 7D, revealed only O (1s), Si (2p), C (1s), and Ag (3d), confirming the high purity of the synthesized materials. The surface composition of each sample, as obtained by XPS, is also shown in Figure 7. The atomic ratio of the elements Si and O is approximately 1:2, in accordance with the silica matrix stoichiometric ratio. These results are similar to those found in the literature.[56,57] MCM-Ag-4-10 presents a higher amount of silver on its surface, in agreement with the ICP-OES results. Nevertheless, the discussed chemical composition is regarding only the material's surface, unlike ICP-OES, which presents the total amount of Ag.

The high-resolution Ag 3*d* spectra – doublets characterized by the 3d 5/2 and 3d 3/2 peaks, with an energy splitting of approx. 6 eV and intensity ratio of 3:2[58] – and the curve fittings are presented in Figure 7E to Figure 7H. Apart from sample MCM-Ag-4-7, where only metallic Ag was identified - 3d 5/2 and 3/2 peaks at 368.3 eV and 374.4 eV, respectively (Figure 7E) - the presence of metallic silver and its more stable oxides, *i.e.* Ag_2O and AgO, was found. The percentage of metallic silver dropped to 60% for MCM-Ag-4, 44% for MCM-Ag-1-10, and 15% for MCM-Ag-4-10 (Figure 7F to Figure 7H, respectively). Although the contributions of the different Ag oxides (AgO, Ag_2O) were not resolved in our analysis, we understand that, for the purposes of this work, it is enough to distinguish the XPS features from metallic silver and those associated with Ag oxides.

The fact that the MCM-Ag-4-7 sample has only metallic silver on its surface, while the MCM-Ag-4 shows an oxidation degree of 40% for Ag, although no NaOH was used during synthesis, suggests that the silver oxide formation can also occur spontaneously on the material's surface due to its constant exposure to atmospheric oxygen. As XPS is a superficial analysis technique, it is not possible to infer the fraction of Ag^0 in the material as a whole. In fact, XRD analysis confirms the presence of metallic silver in the samples. Therefore, the indication of silver oxide on MCM-Ag-4 can be explained by surface oxidation, as suggested by Hund *et al*.[31]

The samples prepared at pH 10, on the other hand, presented a higher oxide concentration, as expected, once NaOH was used during synthesis. By comparing both samples prepared in an alkaline medium, it may be concluded that the highest dose caused greater oxide formation on the material's surface. The higher radiation dose can generate more free radicals during radiolytic synthesis (reducing Ag^+ to Ag^0), which could increase the metallic silver formation. However, a higher concentration of oxide was observed at the sample's surface of the sample submitted to a higher dose exposition.

The nanocomposites surface charges were characterized by zeta potential measurements in water. The mean zeta potential value of MCM-41 was -27.3 mV. The negative value is due to the high amount of silanol groups on the silica's surface. Silanol groups in contact with an aqueous medium and neutral pH ionize, forming SiO^- (Si-OH → Si-O-).[35] All 18 nanocomposites surface charges were measured and they also presented negatively charged surfaces (ZP values between -28 and -20 mV). It indicates that the silver content

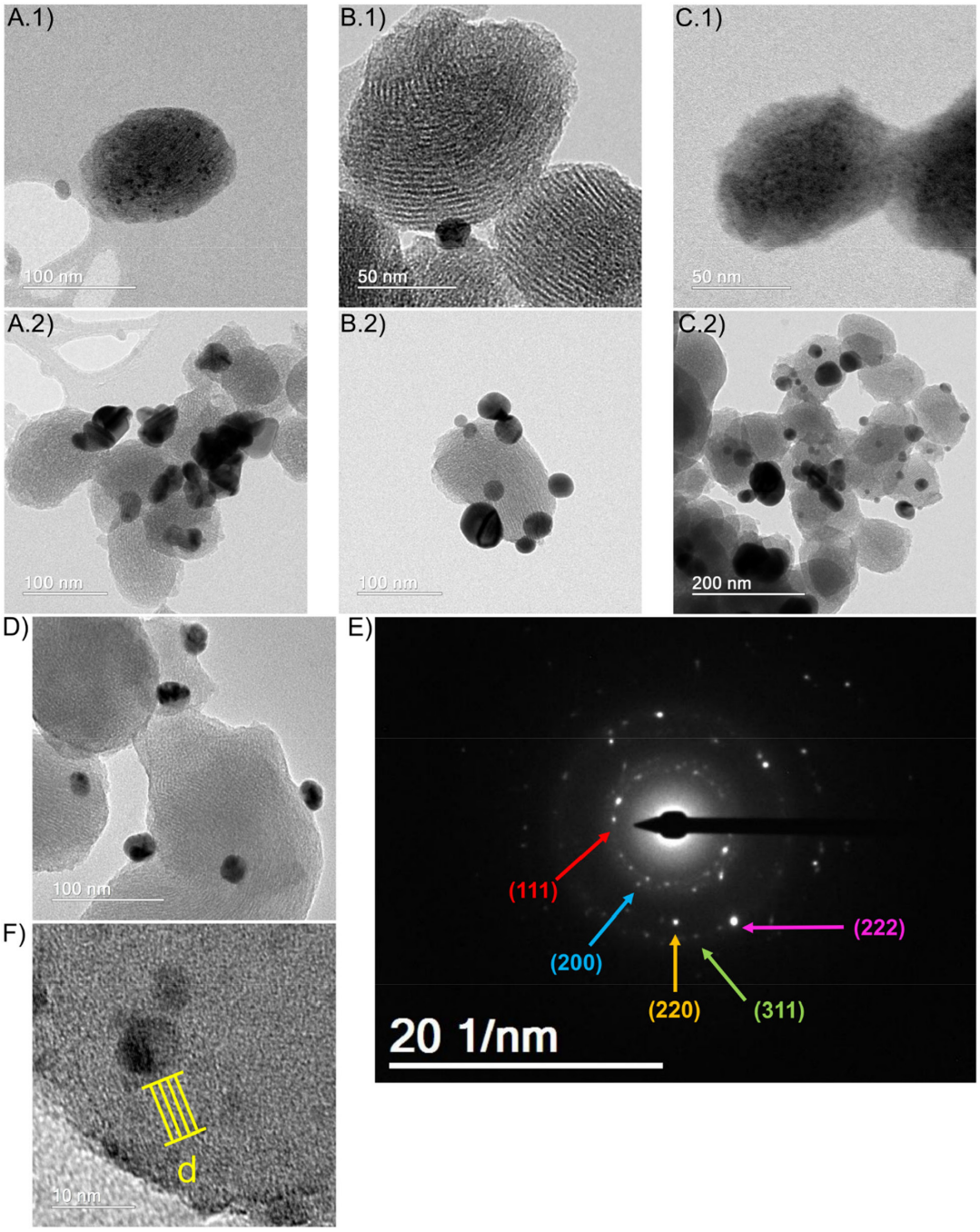

Figure 6. *TEM images of the nanocomposites: A) MCM-Ag-4-7, B) MCM-2Ag-4-7 and C) MCM-Ag-4-10. Images .1 show ultra-small AgNPs (diameter < 5 nm) well dispersed into the matrix and images .2 reveal bigger silver agglomerates with variable sizes. Images D) to F) show MCM-Ag-4: D) reveals a uniform AgNPs size distribution, E) SAED diffraction pattern and F) HRTEM image*

does not change the silanol groups on the matrix surface, as appointed in IR spectroscopy.

Preliminary biological assays were performed in order to study the potential use of nanocomposites in biological conditions. MCM-41 is a biocompatible material, as explored in several works.[35,44] The incorporation of AgNPs on silica's mesopores, on the other hand, can promote nanocomposite cytotoxicity, since the AgNPs released Ag^+. Ag ions can cause reactive oxygen species (ROS) formation, which generates mitochondrial and deoxyribonucleic acid (DNA) damage, leading cells to death.[18] Biocompatibility assays were performed by MTT assay, following the procedures described in the literature,[59] in 6 different nanocomposites and 3 different concentrations (50, 100, and 200 μg mL^{-1}). The results are shown in Figure 8. The nanocomposites tested were: MCM-41 with no Ag content; MCM-Ag-4-7, containing 9.13% of Ag according to the ICP-OES results; MCM-2Ag-4-7, with the greatest Ag content among the samples (21.75%); MCM-2Ag-1-10, presenting 5.96% of Ag content and synthesized in an alkaline medium; 2*MCM-2Ag-1-7, with the lowest Ag content (2.00%) and MCM-Ag-4, with 5.27% of Ag content and with no addition of NaOH.

All materials showed high cell viability (above 80%) up to [200 μg mL^{-1}]. The results did not show statistically significant differences in relation to the control group, indicating biocompatibility and suggesting that MCM-41 encapsulation can protect the cells against AgNPs toxicity. Malekzadeh *et al.* and Oliveira *et al.* tested the cytotoxicity of core-shell Ag@SiO2 nanocomposites with a thin

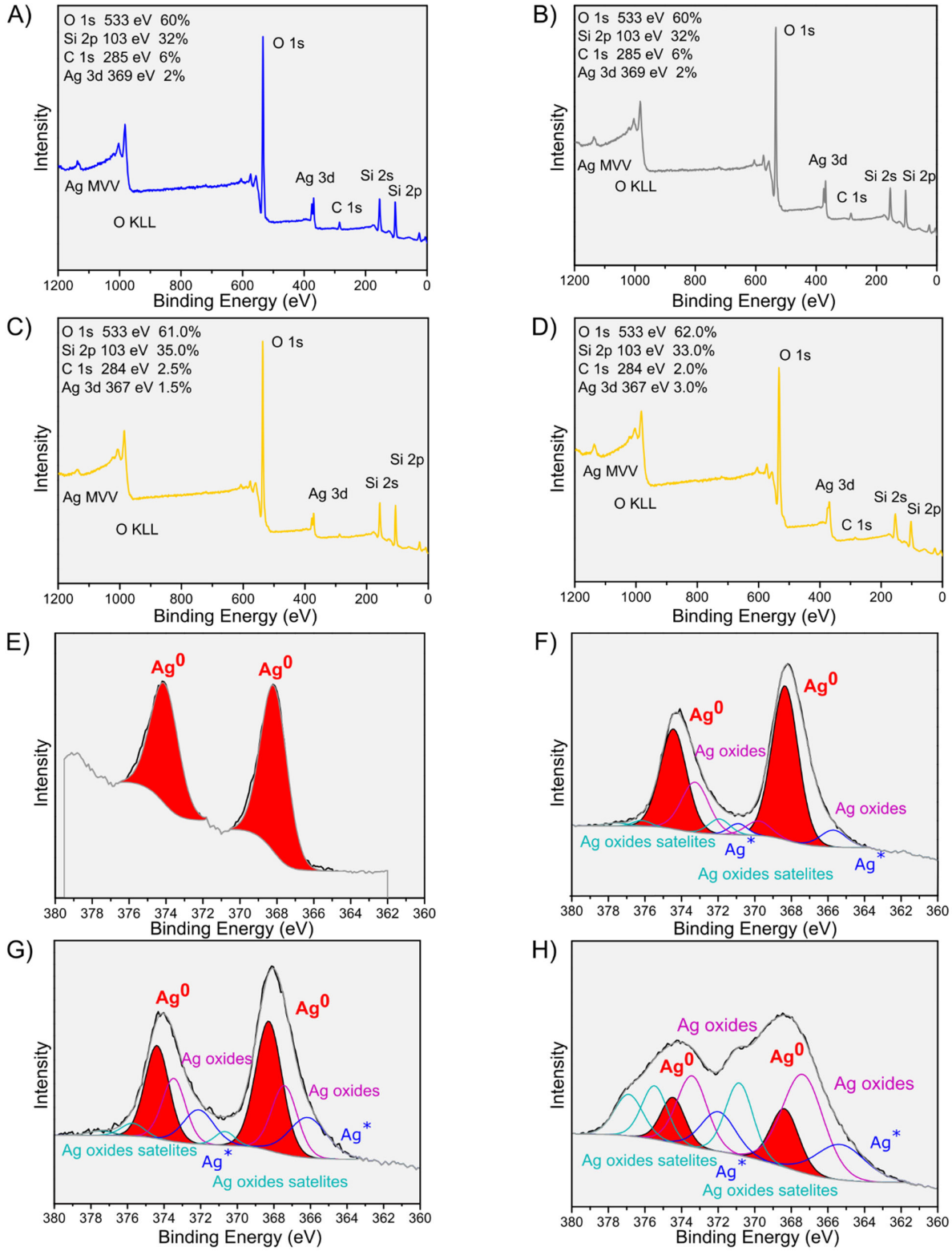

Figure 7. *XPS WS spectra of the nanocomposites: A) MCM-Ag-4-7, B) MCM-Ag-4, C) MCM-Ag-1-10 and D) MCMC-Ag-4-10. XPS high-resolution spectra Ag 3d of the nanocomposites: E) MCM-Ag-4-7, F) MCM-Ag-4, G) MCM-Ag-1-10 and H) MCMC-Ag-4-10. The two Ag^0 peaks are identified in red: 3d 3/2 and 3d 5/2, left to right, respectively*

SiO_2 layer and these systems showed cytotoxicity at concentrations lower than 200 μg mL^{-1}.[5,16] The cytotoxicity of nanoplatforms is influenced by the Ag content (wt%) and the way silver is released from the medium.[18] Despite the MTT viability assay providing only preliminary information regarding biocompatibility, the present work indicates that *in situ* radiolytic synthesis of AgNPs on the MCM-41 matrix can promote higher protection against silver ions releasing. However, a systematic study must be conducted to provide more information about the Ag releasing kinetics, and more advanced biological tests, such as LIVE/DEAD and cell uptaking using a confocal microscope, would be more enlightening about nanomaterial's effect on cells.

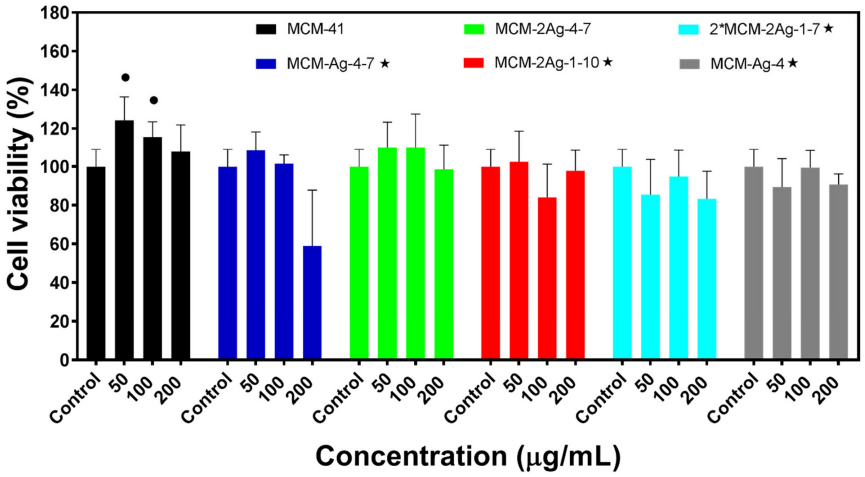

Figure 8. *Cell viability of fibroblasts with different nanocomposites concentrations (50, 100, and 200 μg mL^{-1}) using MTT reagent. Symbols representation: (no symbol) not significant compared to control: P > 0.05; (•) significant in relation to control: 0.01 < P < 0.05; (★) significant in relation to MCM-41*

CONCLUSIONS

In this work, it was presented a statistical study of the AgNPs formation by radiolytic synthesis stabilized by mesoporous silica nanoparticles. A factorial design was created in order to analyze the synthesis parameter effect on the Ag content (wt%) obtained by ICP-OES. The Ag content (wt%) was statically dependent on dose, volume, pH, and the interaction between pH and [Ag^+]. The dose and pH raise promote an increase in the Ag content, while the volume raise, reduces the Ag content. The addition of NaOH during synthesis induces the formation of silver oxides, which was confirmed by XPS analyses when samples synthesized with pH 10 presented a lower Ag (0) % on their surface. However, the presence of metallic FCC silver was confirmed in all tested samples by XRD, including in pH 10. Silver oxides formation occurs despite the NaOH addiction, once Ag is located on the surface is subject to oxidation. Besides the Ag located on the surface, AgNPs were also found inside the silica mesopores, as shown by TEM, which is found in subnanometric nanoparticles with a diameter < 5 nm, and the decrease of the material's SSA with the AgNPs formation. Despite the presence of silver, the nanocomposites presented a great SSA, mesoscopic pore structure, and the silanol group on their surface, confirmed by FTIR and zeta potential analyses. This leads to the conclusion of a potential nanocomposite for further functionalization with other molecules or drugs, once this material is a possible candidate as an antimicrobial substitute. Moreover, preliminary biological assays confirmed the nanocomposites biocompatibility on fibroblast cells up to the concentration of 200 μg mL^{-1}, concluding their potential to fight AMR.

SUPPLEMENTARY MATERIAL

Supplementary material is available at http://quimicanova.sbq.org.br, as a free access PDF file.

ACKNOWLEDGMENTS

This research was supported by the Fundação de Amparo à Pesquisa do Estado de Minas Gerais (FAPEMIG), Conselho Nacional de Desenvolvimento Científico e Tecnológico (CNPq), Coordenação de Aperfeiçoamento de Pessoal de Nível Superior (CAPES) and Comissão Nacional de Energia Nuclear (CNEN). The authors thank the Microscopy Center of the Federal University of Minas Gerais (UFMG), located in Belo Horizonte – Brazil, for the analyses involving electron microscopy and the Biological Science Institute of the same University for the biological assays.

REFERENCES

1. Ukuhor, H. O.; *J. Infect. Public Health* **2021**, *14*, 53. [Crossref]
2. World Health Organization; *Global action plan on antimicrobial resistance*, Geneva, 2015.
3. Wang, Y.; Ding, X.; Chen, Y.; Guo, M.; Zhang, Y.; Guo, X.; Gu, H.; *Biomaterials* **2016**, *101*, 207. [Crossref]
4. Lu, M. M.; Wang, Q. J.; Chang, Z. M.; Wang, Z.; Zheng, X.; Shao, D.; Dong, W. F.; Zhou, Y. M.; *Int. J. Nanomed.* **2017**, *12*, 3577. [Crossref]
5. Malekzadeh, M.; Lun, K.; Halali, M.; Chang, Q.; *Mater. Sci. Eng., C* **2019**, *102*, 616. [Crossref]
6. Gounani, Z.; Asadollahi, M. A.; Pedersen, J. N.; Lyngsø, J.; Pedersen, J. S.; Arpanaei, A.; Meyer, R. L.; *Colloids Surf., B* **2019**, *175*, 498. [Crossref]
7. Capeletti, L. B.; de Oliveira, J. F. A.; Loiola, L. M. D.; Galdino, F. E.; Santos, D. E. S.; Soares, T. A.; Freitas, R. O.; Cardoso, M. B.; *Adv. Funct. Mater.* **2019**, *29*, 1. [Crossref]
8. Yeh, Y. C.; Huang, T. H.; Yang, S. C.; Chen, C. C.; Fang, J. Y.; *Front. Chem.* **2020**, *8*, 1. [Crossref]
9. Kell, A. J.; Stewart, G.; Ryan, S.; Peytavi, R.; Boissinot, M.; Huletsky, A.; Bergeron, M. G.; Simard, B.; *ACS Nano* **2008**, *2*, 1777. [Crossref]
10. Rai, M.; Kon, K.; Gade, A.; Ingle, A.; Nagaonkar, D.; Paralikar, P.; Silva, S. S. In *Antibiotic Resistance*; Rai, M.; Kon, K., eds.; Elsevier Inc.: Amsterdam, 2016, ch. 6.
11. Shurygina, I. A.; Shurygin, M. G.; Sukhov, B. G. In *Antibiotic Resistance*; Rai, M.; Kon, K., eds.; Elsevier Inc.: Amsterdam, 2016, ch. 8.
12. Grumezescu, V.; Holban, A. M.; Barbu, I.; Popescu, R. C.; Oprea, A. E.; Lazar, V.; Grumezescu, A. M.; Chifiriuc, M. C. In *Antibiotic Resistance*; Rai, M.; Kon, K., eds.; Elsevier Inc.: Amsterdam, 2016, ch. 7.
13. Pryshchepa, O.; Pomastowski, P.; Buszewski, B.; *Adv. Colloid Interface Sci.* **2020**, *284*, 87. [Crossref]
14. Wang, Y.; Wang, Y.; Su, L.; Luan, Y.; Du, X.; Zhang, X.; *J. Alloys Compd.* **2019**, *783*, 136. [Crossref]
15. Tian, Y.; Qi, J.; Zhang, W.; Cai, Q.; Jiang, X.; *ACS Appl. Mater. Interfaces* **2014**, *6*, 12038. [Crossref]
16. Oliveira, J. F.; Saito, Â.; Bido, A. T.; Stassen, H. K.; Cardoso, M. B.; *Sci. Rep.* **2017**, *7*, 1. [Crossref]
17. Alsammarraie, F. K.; Wang, W.; Zhou, P.; Mustapha, A.; Lin, M.; *Colloids Surf., B* **2018**, *171*, 398. [Crossref]
18. Liu, J.; Li, S.; Fang, Y.; Zhu, Z.; *J. Colloid Interface Sci.* **2019**, *555*, 470. [Crossref]

19. Belloni, J.; Mostafavi, M. In *Metal Clusters in Chemistry*; Braunstein, P.; Oro, L.A.; Raithby, P.R., eds.; Wiley: Weinheim, 1999, ch. 3.13.
20. De Freitas, L. F.; Varca, G. H. C.; Batista, J. G. dos S.; Lugão, A. B.; *Nanomaterials* **2018**, *8*, 1. [Crossref]
21. Čubová, K.; Čuba, V.; *Radiat. Phys. Chem.* **2019**, *158*, 153. [Crossref]
22. Flores-Rojas, G. G.; López-Saucedo, F.; Bucio, E.; *Radiat. Phys. Chem.* **2020**, *169*, 107962. [Crossref]
23. Das, S.; *Aust J Chem* **2013**, *66*, 522. [Crossref]
24. Belloni, J.; Marignier, J. L.; Mostafavi, M.; *Radiat. Phys. Chem.* **2020**, *169*, 1. [Crossref]
25. Dhayagude, A. C.; Das, A.; Joshi, S. S.; Kapoor, S.; *Colloids Surf., A* **2018**, *556*, 148. [Crossref]
26. Long, D.; Wu, G.; Chen, S.; *Radiat. Phys. Chem.* **2007**, *76*, 1126. [Crossref]
27. Naghavi, K.; Saion, E.; Rezaee, K.; Mahmood, W.; Yunus, M.; *Radiat. Phys. Chem.* **2010**, *79*, 1203. [Crossref]
28. Liu, Y.; Chen, S.; Zhong, L.; Wu, G.; *Radiat. Phys. Chem.* **2009**, *78*, 251. [Crossref]
29. Ramnani, S. P. Ã.; Biswal, J.; Sabharwal, S.; *Radiat. Phys. Chem.* **2007**, *76*, 1290. [Crossref]
30. Sárkány, A.; Sajó, I.; Hargittai, P.; Papp, Z.; Tombácz, E.; *Appl. Catal., A* **2005**, *293*, 41. [Crossref]
31. Hund, J. F.; Bertino, M. F.; Zhang, G.; Sotiriou-leventis, C.; Leventis, N.; Tokuhiro, A. T.; Farmer, J.; *J. Phys. Chem. B* **2003**, *107*, 465. [Crossref]
32. Hornebecq, V.; Antonietti, M.; Cardinal, T.; Treguer-Delapierre, M.; *Chem. Mater.* **2003**, *15*, 1993. [Crossref]
33. Abedini, A.; Daud, A. R.; Hamid, M. A. A.; Othman, N. K.; Saion, E.; *Nanoscale Res. Lett.* **2013**, *8*, 1. [Crossref]
34. Ghoreishian, S. M.; Kang, S.-M.; Raju, G. S. R.; Norouzi, M.; Jang, S.-C.; Yun, H. J.; Lim, S. T.; Han, Y.-K.; Roh, C.; Huh, Y. S.; *Chem. Eng. J.* **2019**, *360*, 1390. [Crossref]
35. Freitas, L. B. O.; Corgosinho, L. de M.; Faria, J. A. Q. A.; dos Santos, V. M.; Resende, J. M.; Leal, A. S.; Gomes, D. A.; de Sousa, E. M. B.; *Microporous Mesoporous Mater.* **2017**, *242*, 271. [Crossref]
36. Vallet-Regi, M.; Rámila, A.; Real, R. P. del; Pérez-Pariente, J.; *Chem. Mater.* **2001**, *13*, 308. [Crossref]
37. Freitas, L. B. O.; Bravo, I. J. G.; Macedo, W. A. de A.; de Sousa, E. M. B.; *J. Sol-Gel Sci. Technol.* **2016**, *77*, 186. [Crossref]
38. Sing, K. S. W.; Everett, D. H.; Haul, R. A. W.; Moscou, L.; Pierotti, R. A.; Rouquerol, J.; Siemieniewska, T.; *Pure Appl. Chem.* **1985**, *57*, 603.
39. Ravikovitch, P. I.; Ó Domhnaill, S. C.; Neimark, A. V.; Schiith, F.; Ungert, K. K.; *Langmuir* **1995**, *11*, 4765. [Crossref]
40. Eustis, S.; El-sayed, M. A.; *Chem. Soc. Rev.* **2006**, *35*, 209. [Crossref]
41. Gasaymeh, S. S.; Radiman, S.; Heng, L. Y.; Saion, E.; Saeed, G. H. M.; *African Physical Review* **2010**, *4*, 31. [Crossref]
42. Minitab®, version 17; Minitab, Inc.; State College, PA, USA, 2017.
43. Nishimura, S.; Mott, D.; Takagaki, A.; Maenosono, S.; Ebitani, K.; *Phys. Chem. Chem. Phys.* **2011**, *13*, 9335. [Crossref]
44. Andrade, G. F.; Lima, G. da S.; Gastelois, P. L.; Gomes, D. A.; Macedo, W. A. de A.; de Sousa, E. M. B.; *Int. J. Appl. Ceram. Technol.* **2020**, *17*, 380. [Crossref]
45. Han, L.; Wei, H.; Tu, B.; Zhao, D.; *Chem. Commun.* **2011**, *47*, 8536. [Crossref]
46. Kresge, C. T.; Leonowicz, M. E.; Roth, W. J.; Vartuli, J. C.; Beck, J. S.; *Nature* **1992**, *359*, 710. [Crossref]
47. Beck, J. S.; Vartuli, J. C.; Roth, W. J.; Leonowicz, M. E.; Kresge, C. T.; Schmitt, K. D.; Chu, C. T.-W.; Olson, D. H.; Sheppard, E. W.; McCullen, S. B.; Higgins, J. B.; Schlenker, J. L.; *J. Am. Chem. Soc.* **1992**, *114*, 10834. [Crossref]
48. Abu-Zied, B. M.; Schwieger, W.; Asiri, A. M.; *Microporous Mesoporous Mater.* **2015**, *218*, 153. [Crossref]
49. Lara, G. G.; Andrade, G. F.; Cipreste, M. F.; da Silva, W. M.; Gastelois, P. L.; Gomes, D. A.; de Miranda, M. C.; Macedo, W. A. A.; Neves, M. J.; de Sousa, E. M. B.; *J. Mater. Sci. Mater. Med.* **2018**, *29*, 130. [Crossref]
50. Pinto, L. M.; Quantikov Image Analyzer v.16.01; Brazil, 2018.
51. Williams, D. B.; Carter, C. B.; *Transmission Electron Microscopy*, 2nd ed.; Springer: New York, 2009.
52. Walther, T. In *Microscopy Methods in Nanomaterials Characterization*; Thomas, S.; Thomas, R.; Zachariah, A. K.; Mishra, R. K., eds.; Elsevier: Amsterdam, 2017, ch. 4.
53. Bois, L.; Chassagneux, F.; Desroches, C.; Battie, Y.; Destouches, N.; Gilon, N.; Parola, S.; Stéphan, O.; *Langmuir* **2010**, *26*, 8729. [Crossref]
54. Guzmán, M. G.; Dille, J.; Godet, S.; *Int. J. Chem. Biomol. Eng.* **2009**, *2*, 104. [Crossref]
55. Kim, B.; Hochella, M. F. In *Characterization of Nanomaterials in Complex Environmental and Biological Media*; Lead, J.; Baalousha, M., eds.; Elsevier: Amsterdam, 2015, ch. 4.
56. Dulski, M.; Laskowska, M.; Sułowicz, S.; Krzykawski, T.; Pastukh, O.; Zieliński, P. M.; Pawlik, P.; Nowak, A.; Laskowski, L.; *Microporous Mesoporous Mater.* **2020**, *306*, 1. [Crossref]
57. John, K.; Peechat, R.; Mathew, S.; *Mater. Today Proc.* **2020**, *33*, 1263. [Crossref]
58. Abbass, A. E.; Van Vuuren, A. J.; Swart, H. C.; Kroon, R. E.; *J. Non-Cryst. Solids* **2017**, *475*, 71. [Crossref]
59. Mosmann, T.; *J. Immunol. Methods* **1983**, *65*, 55. [Crossref]